Characterization of an Aircraft Auxiliary Power Unit Test Rig for Cycle Optimization Studies

Jan Zanger
Institute of Combustion Technology
German Aerospace Center (DLR)
Stuttgart, Germany, 70569
Email: jan.zanger@dlr.de

Thomas Krummrein
Institute of Combustion Technology
German Aerospace Center (DLR)
Stuttgart, Germany, 70569
Email: thomas.krummrein@dlr.de

Teresa Siebel
Institute of Combustion Technology
German Aerospace Center (DLR)
Stuttgart, Germany, 70569
Email: teresa.siebel@dlr.de

Jürgen Roth
Institute of Combustion Technology
German Aerospace Center (DLR)
Stuttgart, Germany, 70569
Email: juergen.roth@dlr.de

Detailed information of the thermodynamic parameters, system performance and operating behavior of aircraft APU cycles is rarely available in literature. In order to set up numeric models and study cycle modifications, validation data with well defined boundary conditions is needed. Thus, the paper introduces an APU test rig based on a Garrett GTCP36-28 with detailed instrumentation which will be used in a further step as a demonstration platform for cycle modifications. The system is characterized in the complete feasible operating range by alternating bleed air load and electric power output. Furthermore, simulations of a validated numerical cycle model are utilized to predict the load points in the operating region which were unstable during measurements. The paper reports and discusses turbine shaft speed, compressor air mass flow, fuel mass flow, efficiencies, compressor outlet pressure and temperature, turbine inlet and outlet temperature as well as exhaust gas emissions. Furthermore, the results are discussed with respect of the difference compared to a Hamilton Sundstrand APS3200. Though the efficiencies of the GTCP36-28 are lower compared to the APS3200, the general behavior is in good agreement. In particular, the effects of separate compressors for load and power section are discussed in contrast to the GTCP36-28 system design comprising a single compressor. In general, it was shown that the GTCP36-28 is still appropriate for the utilization as a demonstration platform for cycle modification studies.

Nomenclature

Abbreviations

APU	Auxiliary Power Unit
CHP	Combined heat and power
VIGV	Variable inlet guide vanes

Latin Letters

AFR	Stoichiometric air-to-fuel ratio [-]
c_p	Heat capacity at p = const. [J/(kg·K)]
H	Relative humidity of the fresh air [% RH]
$\dot{m}_{bl}$	Bleed air mass flow [g/s]

The original publication is available at http://dx.doi.org/10.1115/1.4041119

$\dot{m}_{air}$ Compressor air mass flow [g/s]
$\dot{m}_{cc}$ Combustion chamber air mass flow [g/s]
$\dot{m}_{fuel}$ Fuel mass flow [g/s]
N Turbine shaft speed [rpm]
p Pressure [Pa,abs]
P_{bl} Bleed air power output [kW]
P_{el} Electric power output [kW]
P_{ov} Overall power output [kW]
T Temperature [°C]

Greek Letters
$\lambda_{cc,global}$ Global air number of combustion [-]
Ψ Work coefficient [-]
Φ Flow coefficient [-]
η_{el} Electric efficiency [%]
η_{is} Isentropic efficiency [-]
η_{ov} Overall efficiency [%]

1 Introduction

Auxiliary Power Units (APU) for conventional aircrafts provide electric and pneumatic energy for environmental control system, main engine start and on-board aircraft systems on the ground. Furthermore, they supply emergency power in case of main engine failure during the flight mission. The main requirement for these engines is a high reliability as well as low costs and weight [1]. Thus, electric and overall efficiency of such systems are low resulting in a high relative fuel consumption. Moreover, as studies at the Zurich airport, Switzerland, have shown recent aircraft APUs cause a high air pollution and noise exposure in the airport area [2]. Therefore, local restrictions of APU usage at some airports have been installed. Contradictory to this trend, on-board electric power consumption increases continuously by More Electric Aircraft (MEA) concepts like the Airbus A380 or Boing 787 and higher requirements for passenger comfort [3].

The major difference of aircraft APUs compared to e.g. stationary CHP units is the circumstance that most of the produced power is supplied as pneumatic power. The electric power output has only a minor share. Typically, over 70% of the generated power is supplied as pressurized bleed air mass flow resulting in significant changes of turbine mass flow compared to compressor mass flow. However, with regard to the state of the art of micro gas turbines used in stationary CHP units, there is a high potential of optimizing electric and overall efficiency, exhaust gas emissions and noise radiation of aircraft APU systems. In order to optimize APU systems validated numerical tools of the APU gas turbine cycle based on detailed experimental data as well as an experimental test platform for optimization evaluation tests are necessary.

On behalf of the first, there is a poor availability of experimental data on aircraft APUs in academic literature. Knowledge of operating behavior, internal thermodynamic data and performance envelope is only held at the APU manufacturers [1]. Previously published work on APUs addresses mainly exhaust gas emissions and effects of new types of jet fuels on emission levels. For instance, *Kinsey et al.* [4] measured various gaseous and particular exhaust gas emissions of a GTCP85-98CK installed in a DC-8 aircraft as a function of exhaust gas temperature. They demonstrated a significant reduction of SO_2 and particle mass index by a coal-derived Fischer Tropsch fuel compared to JP-8 fuel. *Ruslan et al.* [5] tested the effects of different novel fuels on smoke number of a GTCP85 APU. On the same engine *Lobo et al.* [6] conducted a systematic evaluation of 16 different blends of alternative fuels at three APU operating conditions. The only available data of cycle performance and thermodynamic process parameters for an aircraft APU is published by *Stohlgren et al.* [7] for a GTCP36-300 APU. On the manufacturer's side *Gorinevsky et al.* [1] discussed model-based diagnostics for offline monitoring the APU status and predicting maintenance need. The authors had access to the wide operational manufacturer's knowledge. Nevertheless, this knowledge is recently unavailable for the academic community.

Therefore, there is need for published experimental data obtained with well-known boundary conditions. In particular, knowledge of operating behavior, internal thermodynamic data and performance envelope in combination with exhaust gas and noise emissions are of major importance. To overcome this situation the German Aerospace Center (DLR) set up an experimental APU test rig in a laboratory environment. The work performed at this system is implemented into a project to study APUs, develop optimization steps like recuperation by means of numerical simulations and evaluate selected optimization steps on the test rig.

In the project's first step a widely used APU system was analyzed as a status quo. Here, the performance and noise emissions of the complete Hamilton Sundstrand APS3200 APU operating range, along with an analysis of the exhaust gas emissions has been previously studied by *Siebel et al.* [8]. In a second step a test rig based on a GTCP36-28 APU system was set up as a demonstration platform and characterized in detail which is reported in the recent publication. A direct comparison of the results of the GTCP36-28 to the previously measured APS3200 data reported by *Siebel et al.* is given in the present paper to evaluate the suitability of the GTCP36-28 as a demonstration platform. In this comparison the APS3200 is used as a reference. By means of the GTCP36-28 data a numerical simulation tool is developed and validated. This tool is used to help interpreting the experimental data. Furthermore, the tool is used for studying changes to the gas turbine cycle with the focus on improving overall efficiency. Additionally, novel concepts of a gas turbine combustor as well as systems for noise reduction are developed and tested on the demonstration platform. The acoustic emission spectra of the original demonstration APU as well as the effects of the newly developed damping measures are addressed by *Knobloch et al.* [9].

The recent publication serves as an introduction to the experimental test rig as demonstration platform and provides a database for numerical simulations of APU cycles. It reports the operating behavior, the performance map in the feasible operating envelope, thermodynamic data inside the gas

The original publication is available at http://dx.doi.org/10.1115/1.4041119

turbine cycle as well as major exhaust gas emissions as a function of the APU load conditions. Furthermore, a comparison to the data of the APS3200 measured by *Siebel et al.* [8] is given in order to evaluate the comparability of the demonstration cycle to a widely used aircraft APU system like the APS3200. Simulated data based on the validated cycle model of the GTCP36-28 is used to describe operating points and process parameters which were not accessible in the measurements.

1.1 GTCP36-28 APU System

The mobile APU test rig is based on a single shaft GTCP36-28 gas turbine APU of Garrett Corporation from the early 1970s. This APU was previously installed in a VFW-614 aircraft. Before storage in the late 1980s the unit was fully refurbished and declared as ready to fly. The GTCP36-28 unit has a length of 0.813 m, a width of 0.597 m and a height of 0.625 m with a dry mass of 88.5 kg. It is equipped with a single stage centrifugal compressor for load and power section comprising a 17 blade impeller without inlet guide vanes generating a pressure ratio of 4.2. The turbine section consists of a single stage radial flow turbine with 13 fix inlet guide vanes and 10 wheel blades. The APU is controlled by a pneumatic/mechanic fuel control unit to a constant turbine speed of 59,200 rpm drooping to 58,000 rpm at high load points. Via a gear box on the compressor side the turbine shaft speed is transformed to a generator shaft of 8,000 rpm shaft speed and 23.5 kW rated shaft power. As installed in the aircraft a separately excited air-cooled Westinghouse generator type 6QM20Q of 20 kVA and a power factor of 0.75 is used on the test rig. Furthermore, a starter motor connected to the gear box accelerates the turbine during start-up. Further engine accessories like the fuel pump and the lubrication module parasite on turbine shaft power via the gear box. A single-stage swirl-stabilized combustor equipped with a pressure atomizer is used in the counter-flow combustion chamber.

Bleed air mass flow is extracted out of the compressor outlet plenum. According to the specifications a minimum bleed air mass flow of 0.388 kg/s can be extracted which corresponds to a bleed air power P_{bl} of approximately 75 kW. The bleed air is regulated by a pneumatic/mechanical load control unit. By activating a magnetic valve in the load control unit the bleed air extraction can be activated. Therefore, the APU can run in two operating modes. In 'no-bleed mode' the load control valve is deactivated and a part of the compressor air flow is bypassed directly into the exhaust gas duct (see fig. 2) to prevent compressor surge. In 'bleed mode' the antisurge valve is deactivated and bleed air can be extracted from the cycle.

The fuel mass flow to the combustor is controlled by a fuel control unit which operates in a completely pneumatic and mechanical way. This unit contains two control loops. In the steady-state operating range a centrifugally driven governor maintains the shaft speed constant and an acceleration limiter is used to adjust the ramp-up gradient during start-up. To prevent damaging excess combustion temperature a pneumatic thermostat located in the exhaust gas duct is activated if exhaust gas temperature exceeds the maximum temperature of 649 °C. In 'bleed mode' this device reduces the bleed-air mass flow in order to keep the exhaust gas temperature within the limits. In 'no-bleed mode' the pneumatic thermostat reduces the fuel mass flow of the acceleration limiter resulting in a reduction of exhaust gas temperature. The reduction of bleed air or fuel mass flow is done by blowing off a small part of compressor mass flow via the thermostat into the exhaust gas duct and therefore, reducing the pressure reference for either the fuel or the load control unit. The switching between both states is controlled by a three way solenoid valve.

2 Experimental and Numerical Setup

2.1 Test Rig

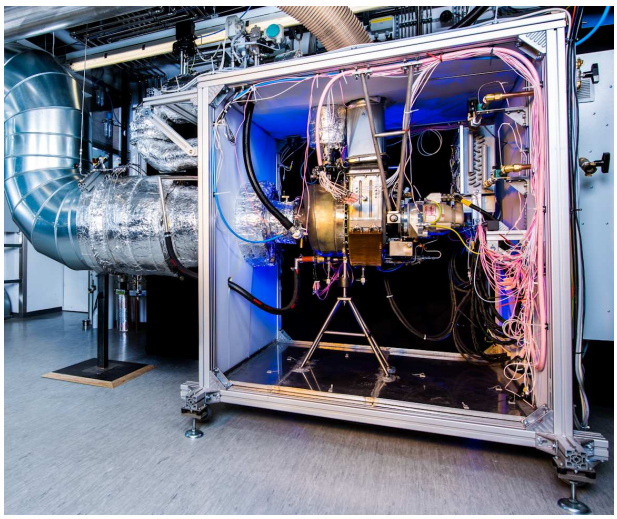

Fig. 1. Mobile APU test rig container

As shown in fig. 1 the GTCP36-28 unit was installed into an enclosed mobile test rig container which is equipped with an air conditioning unit and noise absorbing walls. Fresh air is transported from outside the building via a fine particle filter, a fresh air duct of 219 mm in diameter and a flexible hose to the compressor inlet plenum. The APU exhaust gases are directed via a diffuser to an insulated 324 mm exhaust gas duct. In a distance of approximately 1.5 m to the APU exit an exhaust gas water quench is installed to reduce the exhaust gas temperature below 300 °C preventing stack damage. The layout of the GTCP36-28 cycle as well as the instrumentation relevant for this paper are illustrated in fig. 2. All additional installations in the piping in front and after the APU are symbolized as pressure loss in the cycle layout. The extracted bleed-air is directed via the APU load control unit to a 'Schubert & Salzer (Ingolstadt, Germany) 8021-GS3/8049' pneumatic control valve used as bleed air emulation valve. With the help of this valve defined bleed air mass flows can be adjusted emulating different aircraft bleed

The original publication is available at http://dx.doi.org/10.1115/1.4041119

air loads. Subsequently, the bleed air is fed into the exhaust gas duct in front of the exhaust gas diffuser. The electric power output was alternated by an external resistor load bank from 'Heine Resistors GmbH (Dresden, Germany)'. This load bank can stepwise adjust the generator load from 0 - 20 kW by switchable resistors.

In order to analyze all relevant process parameters detailed instrumentation, including 39 thermocouples, 18 pressure transducers, 3 acoustic sensors and 3 mass flow meters is implemented into the APU cycle. For clarity reasons only the instrumentation relevant for this publication is shown in fig. 2 marked by blank circles with temperature T_i, pressure p_i, inlet air mass flow $\dot{m}_{air}$, bleed air mass flow $\dot{m}_{bl}$, fuel mass flow $\dot{m}_{fuel}$, relative humidity of the fresh air H_0, turbine shaft speed N, electric power output P_{el} and the exhaust gas emissions NO_x, CO, UHC, O_2 and CO_2. The data is acquired at a frequency of 10 Hz and is relayed by multiple 'National Instruments (Austin, USA) CompactRIO' modules, supplying analogue and digital inputs and outputs. The data acquisition modules are situated in a mobile rack connected electrically and pneumatically to the test rig. In the following, all measurement accuracies are specified including the error of data acquisition.

For all temperature measurements except T_0 type N thermocouples (precision class 1 / 1 mm diameter) are used resulting in a maximum error of 4.5 °C for the measured temperature range. The pressures were measured using 'OMEGA Engineering GmbH (Deckenpfronn, Germany) PXM319' transducers of different ranges. The pressure p_0 (see fig. 2) shows a maximum error of $\pm 1.8 * 10^3$ Pa and p_3 possesses a maximum error of $\pm 7.5 * 10^3$ Pa. Each pressure transducer is connected to the point of measurement via a PTFE hose resulting in a time offset of the pressure measurements. Therefore, the external transducers are mainly appropriate for steady-state APU conditions.

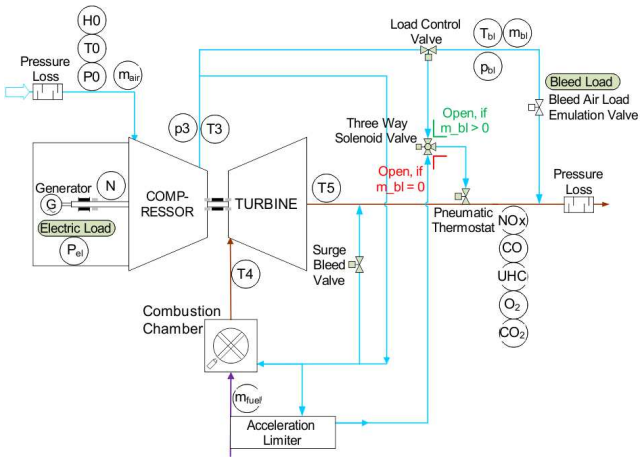

Fig. 2. GTCP36-28 cycle layout and instrumentation

The inlet conditions into the APU system are measured in the fresh air duct. Here, a pressure transducer as well as a 'HX93BC-D' sensor for measuring temperature and relative humidity from 'Omega Engineering GmbH (Deckenpfronn, Germany)' is installed. This temperature T_0 shows a accuracy of ±0.8 °C and the relative humidity is detected with an accuracy of 2.0 %-points RH. The inlet air mass flow $\dot{m}_{air}$ into the APU is measured using a temperature compensated 'AccuFlo-HMP DN200' differential pressure probe from 'SKI GmbH (Mönchengladbach, Germany)' with a relative accuracy of 1.1 %. The bleed air mass flow $\dot{m}_{bl}$ is detected using a 'AccuFlo-HMP DN80' differential pressure probe from 'SKI GmbH (Mönchengladbach, Germany)' with a relative accuracy of 2 %. In this measurement campaign the fuel supply was realized by a 200 liter barrel which was situated next to the test rig container. During the test runs the APU fuel pump primed the fuel directly out of the barrel via a flexible metallic hose and a pickup tube. In this supply line a 'Mini Cori-Flow M15' coriolis mass flow meter from 'Bronkhorst Hightech B.V. (Ruurlo, Netherlands)' with a accuracy of 1.3 % measured the fuel mass flow $\dot{m}_{fuel}$.

In order to analyze the exhaust gas emissions of the APU a multi-hole air cooled gas sample probe was installed into the exhaust gas duct at the same axial position as the pneumatic thermostat. With the help of a mass flow controller the wall temperature of the probe was kept at 299 ± 1 °C maintaining comparable conditions. The exhaust gases were directed via a heated hose of 120 °C to a 'ABB Ltd. (Zürich, Switzerland)' exhaust gas analyzer. In this system NO_x, CO, UHC, O_2 and CO_2 concentrations were detected using UV absorption ('Limas11 HW'), infrared photometry ('Uras26'), flame ionization detection ('Multi FID14') and paramagnetism ('Magnos26'). The detection accuracies of the different species are reported by *Hasemann et al.* [10]. All exhaust gas emissions were corrected to 15 Vol-% O_2 volume fraction and dry conditions.

2.2 Numeric Modeling

The GTCP36-28 is modeled with the MGTS^3 tool. This is a steady state simulation tool for micro gas turbine based processes which is developed at the Institute of Combustion Technology of the DLR. The tool is described in detail in [11–14]. It has a modular structure and contains 0D-models of all system components considering heat and pressure losses.

The acceleration limiter and the pneumatic thermostat are not implemented in the model as they have no effect at steady state conditions. Beside this, all components of fig. 2 are represented in the model. Additionally, the described behavior of 'bleed mode' and 'no-bleed mode' is implemented (see [14]). The pressure loss parameters of components are determined by the experimental data, as well as the parameters of valves and the centrifugal governor.

In MGTS^3 the compressor and the turbine are usually described by turbomachinery maps. In this case no maps could be created by measurement data as the shaft speed can not be set to arbitrary values resulting in an insufficient range of the data points to derive maps. Furthermore, the variation in mass flow and shaft speed in the experimental data is quite small. Due to the harsh environmental conditions and

The original publication is available at http://dx.doi.org/10.1115/1.4041119

Quantity	abs. Deviations mean (min, max)	rel. Deviations mean / %
N in rpm	-8.52 (-547; 464)	-0.011
$\dot{m}_{air}$ in g/s	0.144 (-1.64, 2.18)	0.113
$\dot{m}_{fuel}$ in g/s	0.024 (-0.44, 0.73)	0.319
T_5 in K	2.40 (-12.2, 15.9)	0.42
p_3 in 10^2 Pa	-15.4 (-78.0, 31.7)	-0.41

Table 1. Deviations between the simulation model and measurements with specified bleed air flow and electric output

a significant inhomogeneity of the flow at the turbine inlet a reduced accuracy of the measurements at this position has to be accepted. Therefore, the maps are determined by relations using the work coefficient Ψ, the flow coefficient Φ and the isentropic efficiency η_{is}. For the compressor the work coefficient as well as the isentropic efficiency is described by a second order polynomial of the flow coefficient and the reduced shaft speed. Both polynomials are determined by a regression analysis of the measurement data. As for the turbine the measurement data at the inlet is more error prone only a second order polynomial of the flow coefficient in dependency of the work coefficient is used. The turbine efficiency was assumed as a second order polynomial in dependency of the blade-to-jet velocity ratio $V_r = (2 \cdot \Psi)^{-0.5}$ [15]. Its coefficients were adapted by an optimization process described below. Note that the polynomials describing the turbine are independent of the shaft speed but it is implicitly included in the work coefficient and the flow coefficient.

The heat loss and turbine efficiency polynomial parameters, as well as the generator efficiency and power consumption of the auxiliary units, which include shaft friction losses, are codependent and cannot be directly determined by the measured data. Therefore, the parameters were determined via an optimization process using the overall system model.

All calculated parameters were validated against the measured dataset. Table 1 shows the differences between the model and the measurement data. As the deviations are quite small, the model seems to be suitable to represent the GTCP36-28 in the range of the measurement. Furthermore, all component models are based on physically descriptions. Therefore, also a satisfactory extrapolation behavior is expected. For demonstrating the quality of the validation, the comparison of measured and simulated data is shown in the figures 4, 5 and 7 in the following section. Due to clarity reasons the comparison is only given in the graphs where readability is not disturbed. In all other graphs the deviation is within the limits of table 1 and the trends match well with the measured data.

3 Results

At all load points the parameter calculations were conducted when steady-state conditions of the exhaust gas emissions were achieved since the response of the emissions had the longest time delay of all measured process parameters. In the post-processing calculations all measurement results were averaged over a time span of at least 5 minutes resulting in a total number of single measurement points per load point $\geq$ 3,000. The tests were conducted with standard Jet-A1 delivered by Sasol (Johannesburg, South Africa), where the mass composition of the specific Jet-A1 mixture was analyzed to 0.7% C_7, 3.2 % C_8, 13.8% C_9, 17.7% C_{10}, 17.6% C_{11}, 16.7% C_{12}, 11.4% C_{13}, 9.3% C_{14}, 5.87% C_{15}, 2.4% C_{16}, 0.7% C_{17}. The lower heating value was calculated to 43.195 MJ/kg and the averaged molecular mass was determined to 159.77 g/mol.

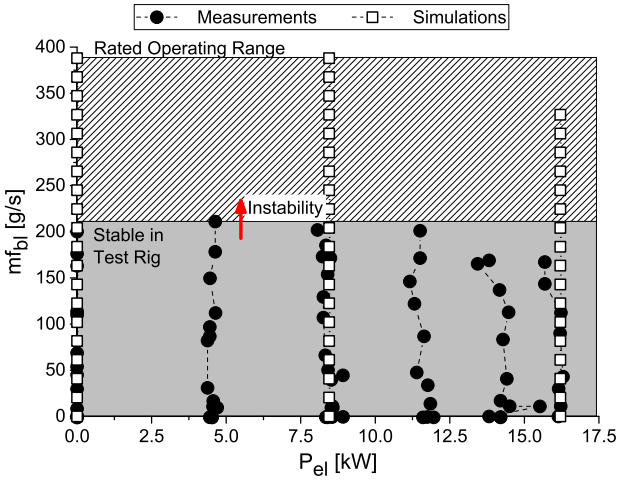

Fig. 3. Operating range of GTCP36-28 APU

In fig. 3 the operating range of the GTCP36-28 is illustrated as a function of electric power output and bleed air mass flow. Electric power output was alternated from 0 to 16.1 kW. The measured load points show a slight shift in the real P_{el}, due to a drift in the generator excitation voltage, as seen clearly in the 16.1 kW case. In the tests only a part of the rated operating range of bleed air mass flow could be run stable. For $\dot{m}_{bl} > 200$ g/s the load points were unstable manifesting itself in a sudden drop of compressor outlet pressure p_3 and a subsequent short increase of compressor inlet pressure. This behavior was accompanied by several loud bangs. Due to the characteristic of this phenomena the authors assume it as compressor surge. The reason for this surge issue at conditions well inside the rated operating range is unclear. An explanation could be a moderate partial damage of some impeller blades due to a strike by a metal connector sucked in during test rig commissioning. To overcome this blind spot the validated simulation model is used to fill the gap. Thus, all parameters shown in the following graphs at operating points $\dot{m}_{bl} > 200 g/s$ are data points simulated by the steady-state model. The simulated data is therefore used to

The original publication is available at http://dx.doi.org/10.1115/1.4041119

extrapolate the measured data and predict the process parameters for the unstable region.

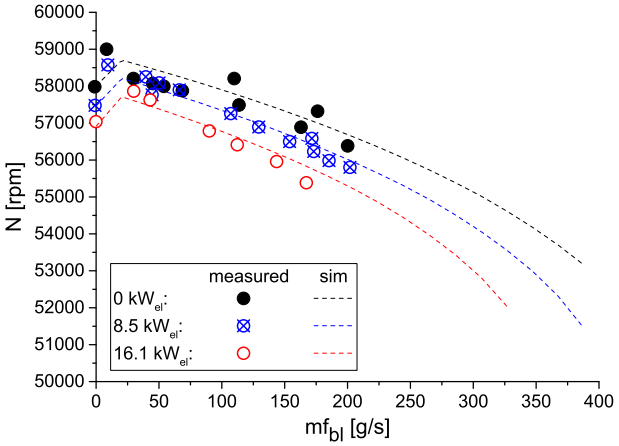

Fig. 4. Turbine shaft speed N as a function of bleed air mass flow $\dot{m}_{bl}$

The turbine shaft speed N of the GTCP36-28 is shown in fig. 4 as a function of $\dot{m}_{bl}$ and P_{el}. For clarity reasons only the data at electric powers of 0 kW, 8.5 kW and 16.1 kW are presented. Furthermore, the simulated shaft speed is visualized for P_{el} = 0 and 16.1 kW in the measured load range showing a very good agreement with the measurements within the deviations of table 1. The measurements at $\dot{m}_{bl}$ = 0 g/s correspond to the 'no-bleed mode' of the APU in which the load control valve is closed and a part of the compressor air is blown off via the surge bleed valve. As soon as the 'bleed mode' is activated the bleed air mass flow jumps to $\approx$ 10 g/s indicating a small air flow via the bleed air load emulation valve. This change of mode is also clearly visible in a jump of turbine speed between $\dot{m}_{bl}$ = 0 g/s and 10 g/s. According to the engine manual the specified turbine speed for 'bleed mode', without bleed load at 59,200 rpm, should decrease to 58,000 rpm at maximum bleed load.

The data in fig. 4 visualizes that the specified turbine speed is achieved well at 10 g/s bleed air mass flow. However, the graph shows a lowest measured speed of 55,400 rpm at P_{el} = 16.1 kW. Regarding the extrapolated simulations the turbine speed would even drop to approximately 51.200 rpm at $\dot{m}_{bl}$ = 400 g/s assuming the same fuel control characteristic for this region. When comparing the speed behavior of all electric power outputs a general decrease of speed with increase of P_{el} and $\dot{m}_{bl}$ is observed. The more pronounced decrease of measured turbine speed compared to the specifications is assumed to be an effect of the centrifugally driven fuel governor being unable to keep the speed within the specified limits. This phenomena leads to a reduced fuel mass flow at high loads as well as a slight change of the operating point of the turbo components. Furthermore, this phenomena could effect the stability of the engine possibly contributing to the instability issue at high bleed air flows.

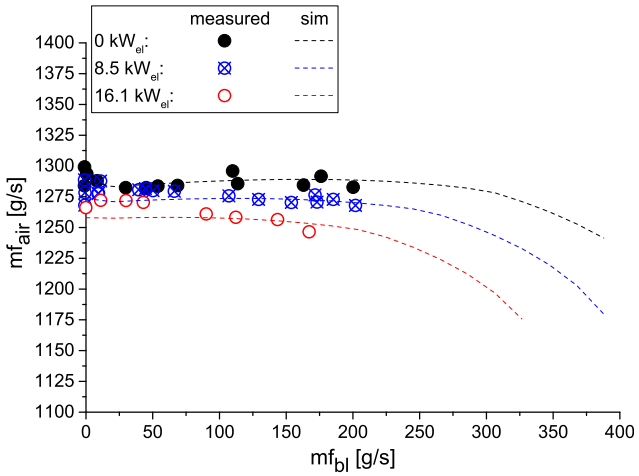

Fig. 5. Compressor air mass flow $\dot{m}_{air}$ as a function of bleed air mass flow $\dot{m}_{bl}$

The effects of the decrease in turbine speed as a function of $\dot{m}_{bl}$ is also observable in the compressor air mass flow $\dot{m}_{air}$ in fig. 5. Here, a corresponding decrease is visible for all electric power outputs. As the decrease of turbine speed is more pronounced for increasing P_{el} the behavior is the same for the decrease of $\dot{m}_{air}$. At the highest electric power of 16.1 kW the air mass flow drops from initially 1270 g/s to 1245 g/s at $\dot{m}_{bl}$ = 165 g/s resulting in simulated 1180 g/s at $\dot{m}_{bl}$ = 325 g/s. The difference between the profiles of constant P_{el} even enlarges for higher $\dot{m}_{bl}$. The decline of each profile at constant P_{el} shows a exponential trend. In order to evaluate the quality of the simulation model the simulated compressor air mass flow is additionally shown in fig. 5 for P_{el} = 0 and 16.1 kW in the measured load range. Here, a good agreement to the measurement data of both the profiles as well as the magnitudes is visible having a relative deviation corresponding to table 1. Since the simulation model is strictly based on physically descriptions, the declining trend of the simulated air mass flow is believed to be reliable qualitatively.

The fuel mass flow $\dot{m}_{fuel}$ of the GTCP36-28 APU is visualized in fig. 6 as a function of overall power output P_{ov}. Based on the equations provided by *Siebel et al.* [8] the overall power output is defined as

$$P_{ov} = P_{el} + P_{bl} \tag{1}$$

whereas the bleed air power P_{bl} is determined by

$$P_{bl} = \dot{m}_{bl} \cdot c_p (T_3 - T_0) \tag{2}$$

In order to clarify the general trends the profiles of all conducted P_{el} are shown in this graph. Additionally to the profiles at constant P_{el}, a linear fit for the load points at 'no-bleed mode' is illustrated in dashed black line and the fit at 'bleed mode' in solid black line. All data points of the simulated region ($\dot{m}_{bl} > 200$ g/s) are symbolized in blank black dots. In the graph two distinctly separated areas are visible. The main

The original publication is available at http://dx.doi.org/10.1115/1.4041119

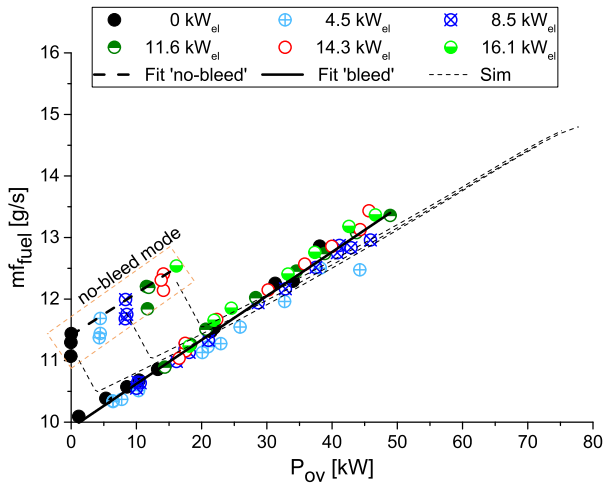

Fig. 6. Fuel mass flow $\dot{m}_{fuel}$ as a function of overall power output P_{ov}

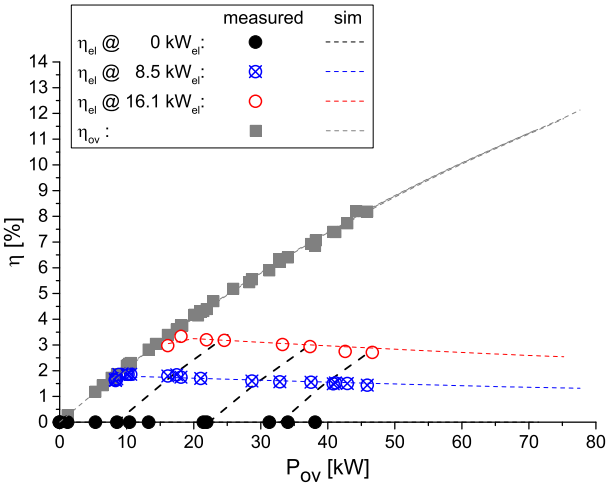

Fig. 7. Electric η_{el} and overall η_{ov} efficiency as a function of overall power output P_{ov}

part of the load points of all P_{el} collapse into one curve starting at $\dot{m}_{fuel}$ = 10 g/s and rising up to 15 g/s. This curve represents the load points at 'bleed mode'. This curve can be described by a linear fit of $\dot{m}_{fuel}\,(bleed) = 0.0714 \cdot \dot{m}_{bl} + 9.908$ with a corrected R^2 of 0.97. This means that the APU fuel mass flow is only a function of overall power output at 'bleed mode'. The smaller subsection of the load points, which is situated above, corresponds to the 'no-bleed mode'. These data points show a wider variation correlating with the compressor inlet temperature T_0 and the turbine shaft speed N. For the points with the lowest $T_0 = 4.1 \pm 0.88$ °C a linear regression is given by $\dot{m}_{fuel}\,(no\text{-}bleed) = 0.0681 \cdot \dot{m}_{bl} + 11.412$ with a corrected R^2 of 0.99. Thus, both fits have an almost parallel run with a significant offset to higher fuel mass flows for the 'no-bleed mode'. This shows that 'no-bleed mode' is far off the design point of the GTCP36-28.

This finding is in accordance with the results of the APS3200 APU [8] having a strictly linear trend as well. However, this pronounced offset at 'no-bleed mode' was not visible for the APS3200. Hence, in terms of $\dot{m}_{fuel}$ both APUs behave very similar in 'bleed mode' which is the main operating mode of APUs. Since a minimum bleed air mass flow of 940 g/s could be extracted from the APS3200 a direct comparison of 'bleed mode' to 'no-bleed mode' was prevented for that APU. Even though all 'bleed mode' data points of the GTCP36-28 APU collapse into one curve as a function of P_{ov}, the same data points show distinctly separated profiles for constant P_{el} when drawn as a function of $\dot{m}_{bl}$ (not shown here). These profiles are stacked with respect to the electric power output, leading to higher $\dot{m}_{fuel}$ at higher P_{el}.

In fig. 7 both the electric efficiency η_{el} and the overall efficiency η_{ov} are shown as a function of P_{ov}. Following *Siebel et al.* [8] the electric efficiency is defined as

$$\eta_{el} = \frac{P_{el}}{\dot{m}_{fuel} \cdot H_{u,JetA1}} \tag{3}$$

where the lower heating value is given as $H_{u,JetA1}$ = 43.26 MJ/kg for Jet-A1. Corresponding to the same publication the overall efficiency η_{ov} is determined by

$$\eta_{ov} = \frac{P_{ov}}{\dot{m}_{fuel} \cdot H_{u,JetA1}} \tag{4}$$

Furthermore, the dashed grey lines in fig. 7 symbolize lines of constant bleed air power. Since the APU generates both electric power and bleed air power, the magnitude of the electric efficiency is poor compared to the overall efficiency. Additionally, the electric efficiency of all electric power outputs show a decreasing trend for increasing P_{ov} and increasing bleed air mass flow, respectively. For instance at P_{el} = 16.1 kW η_{el} declines continuously from 3.3% at P_{ov} = 16 kW to 2.5% at P_{ov} = 75 kW. The reason for this behavior is the increase in fuel mass flow for rising P_{ov} simultaneously keeping the electric power output constant. The conditions at 'no-bleed mode' are evident in a drop of approximately 0.35% in η_{el} at the left end of all profiles. The drop in η_{el} is due to the increase in $\dot{m}_{fuel}$ at 'no-bleed mode' as discussed in fig. 6. Comparing the results of the GTCP36-28 to the APS3200 APU [8] the same asymptotic trend of the curves at constant bleed air power are evident. Additionally, the decline of electric efficiency for increasing P_{ov} was also observed at the APS3200 APU. However, the magnitude of maximum η_{el} of the APS3200 is with 8.4% more than 2 times higher than for the GTCP36-28. In spite of the different efficiency magnitudes both APUs behave comparable in terms of η_{el}.

Regarding the overall efficiency all data points of the GTCP36-28 APU collapse into one asymptotic curve with the equation $\eta_{ov} = 20.602 - 20.553 \cdot 0.989^{P_{ov}}$ showing a corrected R^2 of 0.999. The maximum η_{ov} at maximum P_{ov} reaches 12.1% at a P_{bl}-to-P_{el}-ratio of 4.6. Comparing both APUs the maximum overall efficiency of the APS3200 (see [8]) is with 21.4% only 1.5 times higher than the GTCP36-28 efficiency. Furthermore, the η_{ov}-profiles of the APS3200

The original publication is available at http://dx.doi.org/10.1115/1.4041119

show a distinct separation for different bleed loads. This behavior is an effect of the difference in APU system design. Where the GTCP36-28 has only one compressor resulting in a continuous profile of η_{ov}, the APS3200 is equipped with two separate compressors for load and power section. Additionally, variable inlet guide vanes (VIGV) are implemented in front of the APS3200 load compressor to adjust the compressor efficiency. Owing to the installation of VIGVs, the efficiency profiles at different bleed air loads are adjusted.

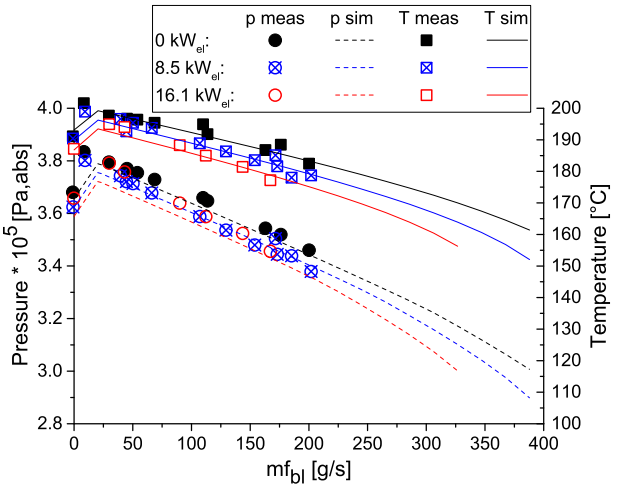

Fig. 8. Compressor outlet pressure p_3 and temperature T_3 as a function of bleed air mass flow $\dot{m}_{bl}$

In fig. 8 the compressor outlet pressure p_3 and temperature T_3 are visualized as a function of bleed air mass flow. Both variables show a strictly decreasing trend. Furthermore, the variables are only minor dependent of P_{el}. For T_3 a slight stacked arrangement of the P_{el} profiles is given whereas the difference of the curves is in the order of 3 K in the measured operating range. The temperature declines from 200 °C at $\dot{m}_{bl}$ = 10 g/s to 150 °C at $\dot{m}_{bl}$ = 325 g/s. The bleed air outlet temperature T_{bl} is related to the compressor outlet temperature by the equation, $T_3 - T_{Bl} = -0.0736 \cdot \dot{m}_{bl} + 2.786$, where the maximum difference reach only 10 K. Since the compressor outlet plenum is directly connected to the combustion chamber inlet there is only a minor decrease of temperature by -15 K due to the uninsulated walls of the compressor plenum.

The pressure p_3 declines from $3.83 \cdot 10^5$ Pa(abs) at $\dot{m}_{bl}$ = 10 g/s to $3.0 \cdot 10^5$ Pa(abs) at $\dot{m}_{bl}$ = 325 g/s. Owing to the pressure drop from the load control valve, the bleed air static pressure is approximately $0.1 \cdot 10^5$ Pa(abs) below p_3. The accurate correlation between both pressures is $p_3 - p_{Bl} = -2.174 \cdot \dot{m}_{bl} + 0.077$. The pressure drop between p_3 and the combustion chamber inlet is negligible. In the pressure profiles of fig. 8 a significant drop by $0.2 \cdot 10^5$ Pa(abs) at 'no-bleed mode' is evident. The drop is due to the extent of the surge bleed valve opening, bleeding an air mass flow of approximately 90 g/s (according to the simulations) from the compressor plenum directly into the exhaust gas duct. This drop of pressure at 'no-bleed mode' corresponds well to the measured pressure p_3 at $\dot{m}_{bl}$ = 90 g/s in 'bleed mode'.

The turbine inlet temperature T_4 and the turbine outlet temperature T_5 are visualized in fig. 9 as a function of $\dot{m}_{bl}$. The measurements of both temperatures represent rather qualitative indications of the real temperature due to a very strong temperature inhomogeneity of the exhaust gas flow at turbine inlet and outlet. The temperature T_5 is arithmetically averaged over 4 temperature measurement positions which show a variation of ± 25 K. At the temperature position T_4 only one of the 4 installed thermocouples remained intact. Therefore, no information about the spatial temperature variation is available. However, the authors assume it at minimum of the same order as the variation of T_5. Since the general trends of both temperatures are consistent as a function of $\dot{m}_{bl}$ the qualitative behavior is believed to be correct. The simulated temperature T_4 is calculated by the enthalpy difference resulting in a complete conversion of Jet-A1. Furthermore, additional thermal losses between combustion chamber and compressor outlet, compressor outlet and APU enclosure as well as bleed air and ambient conditions are considered in the calculation. The losses are modeled as $\propto (T_{hot} - T_{cold})$.

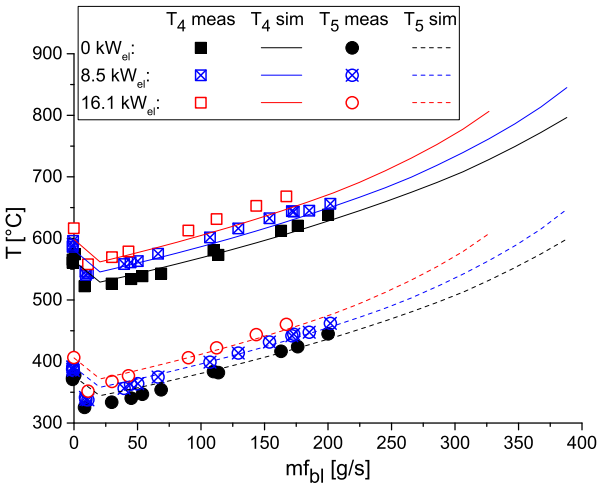

Fig. 9. Turbine inlet T_4 and outlet temperature T_5 as a function of bleed air mass flow $\dot{m}_{bl}$

Both temperatures show the same almost linear trend. Additionally, a stacked arrangement as a function of P_{el} is visible resulting in approximately 50 K higher temperatures for 16.1 kW compared to 0 kW. At 16.1 kW the temperature T_4 increases from 550 °C at $\dot{m}_{bl}$ = 10 g/s to 800 °C at $\dot{m}_{bl}$ = 325 g/s. The strong increase in turbine inlet temperature at 'no-bleed mode' to 615 °C corresponds well to the temperature at $\dot{m}_{bl}$ = 90 g/s. This behavior confirms the simulation results showing an air mass flow via the surge bleed valve of approximately 90 g/s. For the same electric power output the turbine outlet temperature T_5 increases from 350 °C at $\dot{m}_{bl}$ = 10 g/s to 600 °C at $\dot{m}_{bl}$ = 325 g/s.

Comparing the turbine outlet temperature range of the

The original publication is available at http://dx.doi.org/10.1115/1.4041119

GTCP36-28 to the range of the APS3200 [8] the same span is covered. The exhaust gas temperature of the APS3200 ranges from 350 °C to 520 °C showing the same trends. The only difference observed is a shift of the temperature profiles at different bleed air loads. As discussed before, this is also an effect of the APS3200 design equipped with a separate load compressor and VIGVs. Apart from the VIGV influence the trends of the main APU parameters $\dot{m}_{fuel}$, η_{el}, η_{ov} and turbine outlet temperature as well as the APU's control strategy match very well between GTCP36-28 and APS3200. Due to these similarities the GTCP36-28 is found to be suitable as a demonstration platform for APU cycle modifications such as recuperated cycles or operation with variable shaft speeds.

3.1 Exhaust gas emissions

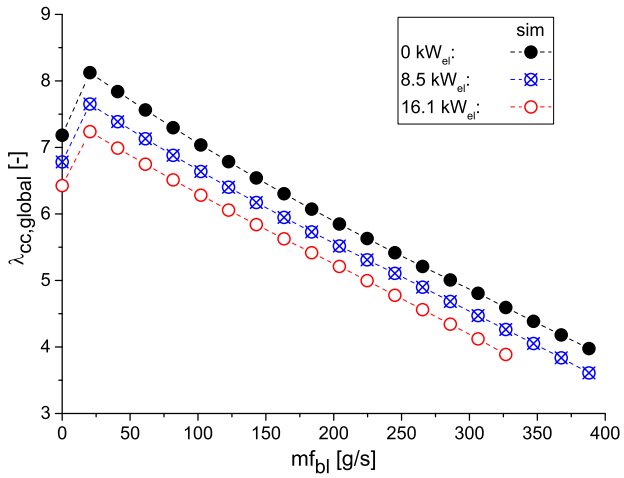

Fig. 10. Global air number $\lambda_{cc,global}$ of the combustion chamber as a function of bleed air mass flow $\dot{m}_{bl}$

In order to explain the observed trends of the exhaust gas emissions (see fig. 11), the global air number inside the combustion chamber is visualized in fig. 10 as a function of $\dot{m}_{bl}$. The air number, which is the reciprocal of the equivalence ratio, is calculated by the balance of the air mass flow into the combustion chamber $\dot{m}_{cc}$ and the fuel mass flow $\dot{m}_{fuel}$:

$$\lambda_{cc,global} = \frac{\dot{m}_{cc}}{\dot{m}_{fuel} \cdot AFR} \tag{5}$$

Since $\dot{m}_{cc}$ was not directly accessible for the measurements $\dot{m}_{cc}$ and $\dot{m}_{fuel}$ were taken from the cycle simulations for calculating $\lambda_{cc,global}$. The stoichiometric air-to-fuel ratio AFR of the utilized Jet-A1 is calculated to 14.58 by the fuel supplier. From the global air number, the complete air which is inserted into the combustion chamber, is described. This means that not only the air taking part in the combustion process but also air which is used as dilution or cooling air is included in this number. Thus, the unknown local air number in the combustion region is much lower. Nevertheless, the general trends should match.

The $\lambda_{cc,global}$ profiles show a non-linear decrease from 7.2 at $\dot{m}_{bl}$ = 10 g/s to 3.9 at 325 g/s for P_{el} = 16.1 kW. The range of the global air number indicates that the combustion needs to be stabilized in a very wide operating range. Additionally, the profiles exhibit a distinct stacked arrangement with lower air numbers at increasing P_{el}. The observed behavior of the global air number is used in the following to interpret the measured exhaust gas emissions.

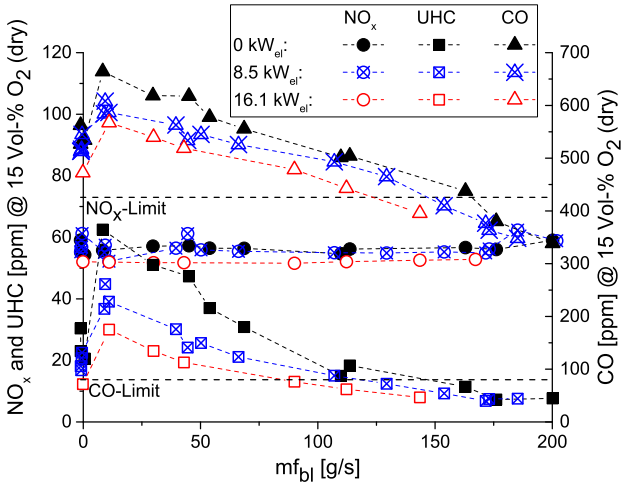

Fig. 11. NO_x, CO and UHC exhaust gas emissions as a function of bleed air mass flow $\dot{m}_{bl}$

In fig. 11 the exhaust gas emissions NO_x, CO and UHC are shown as a function of bleed air mass flow in the stable operating range. All emissions are normalized to 15 Vol-% O_2 at dry conditions. Presently, there are no ICAO regulations [16] applicable to APUs. However, exhaust gas emissions during ground aircraft operations are an issue at major airports [2, 17]. In order to evaluate the measured emissions of the GTCP36-28 the German regulations for gas turbine CHP units for stationary power supply are used as a reference [18]. This gives the opportunity to compare the combustion system to recent gas turbine systems in the field of stationary power supply. The regulated emission limits of CO and NO_x for gas turbine CHP units with less than 50 MW thermal liquid fuel power are shown in the graph as horizontal dashed lines.

The CO emission profiles of the GTCP36-28 exhibit a nearly linearly decreasing trend in the measured $\dot{m}_{bl}$ range. However, the CO magnitude is very high with 665 ppm at $\dot{m}_{bl}$ = 10 g/s and 340 ppm at $\dot{m}_{bl}$ = 200 g/s for P_{el} = 0 kW. These emissions are far above the CO limit of 80 ppm defined by the German CHP unit regulation. Furthermore, a stacked arrangement can be observed for different electric power outputs resulting in a decrease of CO emissions by increasing P_{el}. In general, CO emission levels are a strong function of combustion temperature and residence time. In the GTCP36-28 combustion chamber both effects, residence

The original publication is available at http://dx.doi.org/10.1115/1.4041119

time and combustion temperature, contribute to the CO decreasing trend at rising bleed air flow. On the one hand the residence time is a function of combustion chamber air mass flow $\dot{m}_{cc}$ and gas temperature. With an increasing $\dot{m}_{bl}$ the $\dot{m}_{cc}$ is reduced since air mass flow is extracted out of the gas turbine cycle. Thus, the residence time of the hot gases inside the combustion chamber increases with rising $\dot{m}_{bl}$ at constant electric power output. Hence, the conversion progress of CO to CO_2 proceeds further towards equilibrium conditions. On the other hand the air number inside the combustion chamber decreases as shown in fig. 10. This behavior leads to an increase in combustion temperature by conditions closer to stoichiometry. CO emissions of gas turbine combustion are mostly defined by non-equilibrium effects [19] due to insufficient residence time in the combustion chamber. In this non-equilibrium branch of the CO profiles an increase in combustion temperature leads to a reduction of CO emissions [20]. Using this assumption both effects, increase in residence time and higher combustion temperature, contribute to a better conversion of CO to CO_2 resulting in a decrease of CO emissions with rising $\dot{m}_{bl}$.

Additionally, the stacked arrangement of the CO profiles at different P_{el} can be explained by a similar train of thought. The air mass flows at constant $\dot{m}_{bl}$ do not change significantly at varying P_{el} rates (see fig. 5). Therefore, the residence time is assumed to be dominated by the temperature effect. However, $\lambda_{cc,global}$ decreases and combustion temperature increases, respectively, with rising electric power output. This results on the one hand in a reduction in residence time due to a higher volume flow. On the other hand the combustion process is enhanced due to the higher combustion temperature intensifying the CO conversion. Since a reduction of CO emission level by increasing P_{el} is observed the dominating effect seems to be the enhanced CO conversion by higher combustion temperature.

The UHC emission profiles show the same behavior as described for CO having the same reasons for these characteristics. Though, the UHC profiles exhibit a parabolic trend with a distinctly stacked arrangement at low bleed air mass flow and a converging run at high $\dot{m}_{bl}$.

The NO_x emissions of the GTCP36-28, which were calculated by the sum of NO and NO_2, are nearly constant between 50 and 60 ppm in the complete $\dot{m}_{bl}$ range. This magnitude is below the limit value of 73 ppm defined for the stationary CHP units powered with liquid fuel. However, these magnitudes are still high compared to state-of-the-art [21] and novel liquid fuel combustors [22]. These combustion systems exhibit NO_x emissions down to single digit levels. Though macro scale effects of the mass flow and temperature take place in the GTCP36-28 combustion chamber, the NO_x emissions are constant in the complete operating range. Even though the thermal NO_x formation process is highly sensitive to temperature variation. This means that small scale effects near the spray droplets seem to dominate the NO_x formation. In the droplet surrounding area a near-stoichiometric vapor/air mixture often forms leading to a high NO_x formation. This behavior indicates a poor atomization of the fuel and a low mixing with combustion air.

Comparing the emissions of the GTCP36-28 with those of the APS3200 [8] a different trend can be observed by increasing bleed load. Where the CO emissions of the GTCP36-28 decrease, the APS3200 show an increase by rising $\dot{m}_{bl}$. The authors assume this behavior to be an effect of the different APS3200 mass flow characteristics, due to the two compressor design. Furthermore, the CO levels are with a maximum of 140 ppm much lower than those of the GTCP36-28. The same increasing trend for rising bleed load was seen for the NO_x profiles of the APS3200 having the same explanation as the CO behavior. In contrast to the CO levels the NO_x emissions of the APS3200 exceed the GTCP36-28 values with a maximum of 102 ppm.

4 Summary and Conclusions

A GTCP36-28 APU test rig was set up at the German Aerospace Center (DLR) in Stuttgart. The rig is utilized as a validation system for APU cycle simulation models and as a demonstration platform for cycle optimization studies. The paper introduced the rig, the APU and the instrumentation. In order to close the gap in available APU performance and cycle data a detailed characterization of the APU was performed in the feasible operating range. Thus, this publication provided a detailed dataset for APU model validation. Furthermore, a comparison of the measured data to the data of a Hamilton Sundstrand APS3200 APU [8] was given, evaluating the GTCP36-28 system performance and behavior.

Stable operation was only feasible in half of the rated operating range. A combination of a partly damaged impeller and an undesired behavior of the fuel governor is assumed to cause the instabilities at higher bleed air mass flow. Thus, the validated model was used to predict the trends in the region not accessible for the measurements. In general, both the electric and the overall efficiency of the GTCP36-28 are low. The electric efficiency shows a maximum of 3.3%, where the overall efficiency, which includes the bleed air power, exhibits a maximum of 12%. Furthermore, the exhaust gas emissions of the GTCP36-28 show high CO ($>$ 300 ppm) and UHC (peak $UHC >$ 60 ppm) levels as well as moderate NO_x magnitudes ($>$ 50 ppm) indicating a low burnout.

In general a similar behavior is evident for both APUs, GTCP36-28 and APS3200 [8]. The similarity expresses itself in comparable trends of overall and electric efficiency as well as air and fuel mass flows. The main difference between the characteristics of both APUs is the influence of the two-compressor design of the APS3200. The design with separated compressors for load and power section and variable inlet guide vanes at the load compressor leads to a stacked arrangement of the efficiency profiles for various bleed air mass flows. On the contrary, all GTCP36-28 profiles collapse into one curve.

The contrast of GTCP36-28 and APS3200 shows that the general operating behavior of both APUs is in good agreement. Even though the still widely used APS3200 comprises more recent technology e.g. two compressors for load and power section or electronic fuel controllers, due to the similar system behavior the GTCP36-28 is found to be ap-

The original publication is available at http://dx.doi.org/10.1115/1.4041119

propriate as a demonstration platform for cycle innovations. The efficiency level of the GTCP36-28 is well below state-of-the-art APU technology. Nevertheless, the GTCP36-28 system can be used to demonstrate the relative quantitative effects of modification steps such as recuperation or variable turbine speed at part load. In the next step the demonstration platform will be used to validate these off-design studies and evaluate the benefits of recuperation for the given APU cycle.

Acknowledgements

The authors would like to thank the whole APU project team for the fruitful discussions. In particular, the expertise of Darvid Huhn in planning, coordinating and bug fixing the electronics and data acquisition is highly acknowledged. Furthermore, the authors thank Ralph Bruhn for all the welding work at the rigs infrastructure.

References

[1] Gorinevsky, D., Dittmar, K., Mylaraswamy, D., and Nwadiogbu, E., 2002. "Model-based diagnostics for an aircraft auxiliary power unit". In Proceedings of the International Conference on Control Applications, Vol. 1, pp. 215–220 vol.1.

[2] Fleuti, E., and Hofmann, P., 2005. Aircraft APU emissions at Zurich airport. Tech. rep., Unique Flughafen Zürich.

[3] Roboam, X., Sareni, B., and Andrade, A. D., 2012. "More electricity in the air: Toward optimized electrical networks embedded in more-electrical aircraft". *IEEE Industrial Electronics Magazine,* **6**(4), Dec, pp. 6–17.

[4] Kinsey, J. S., Timko, M. T., Herndon, S. C., Wood, E. C., Yu, Z., Miake-Lye, R. C., Lobo, P., Whitefield, P., Hagen, D., Wey, C., Anderson, B. E., Beyersdorf, A. J., Hudgins, C. H., Thornhill, K. L., Winstead, E., Howard, R., Bulzan, D. I., Tacina, K. B., and Knighton, W. B., 2012. "Determination of the emissions from an aircraft auxiliary power unit (APU) during the alternative aviation fuel experiment (AAFEX)". *Journal of the Air & Waste Management Association,* **62**(4), pp. 420–430.

[5] Ruslan, M., Ahmed, I., and Khandelwal, B., 2016. "Evaluating effects of fuel properties on smoke emissions". In Proceedings of ASME Turbo Expo, no. GT2016-56791, Seoul, South Korea, June 13 -17, 2016.

[6] Lobo, P., Christie, S., Khandelwal, B., Blakey, S. G., and Raper, D. W., 2015. "Evaluation of non-volatile particulate matter emission characteristics of an aircraft auxiliary power unit with varying alternative jet fuel blend ratios". *Energy,* **29**, pp. 7705 – 7711.

[7] Stohlgren, L., and Werner, L. D., 1986. "The GTCP36-300, a gas turbine auxiliary power unit for advanced technology transport aircraft". In Proceedings of the International Gas Turbine Conference and Exhibit, no. 86-GT-285, Düsseldorf, Germany, June 8 - 12, 1986.

[8] Siebel, T., Zanger, J., Huber, A., Aigner, M., Knobloch, K., and Bake, F., 2018. "Experimental investigation of cycle properties, noise and air pollutant emissions of an APS3200 auxiliary power unit". *Journal of Engineering for Gas Turbines and Power,* **140**(061201), pp. 1 – 9.

[9] Knobloch, K., Enghardt, L., and Bake, F., 2018. "APU-noise reduction by novel muffler concepts". In Proceedings of ASME Turbo Expo, no. GT2018-76762, Oslo, Norway, June 11 - 15, 2018.

[10] Hasemann, S., Huber, A., Naumann, C., and Aigner, M., 2017. "Investigation of a FLOX-based combustor for a micro gas turbine with exhaust gas recircuulation". In Proceedings of ASME Turbo Expo 2017, no. GT2017-64396, Charlotte, USA, June 26 - 30, 2017.

[11] Panne, T., Widenhorn, A., Boyde, J., Matha, D., Abel, V., and Aigner, M., 2007. "Thermodynamic process analyses of SOFC/GT hybrid systems". In AIAA Paper No. 2007-4833.

[12] Henke, M., Monz, T., and Aigner, M., 2013. "Inverted Brayton cycle with exhaust gas recirculation - a numerical investigation". *Journal of Engineering for Gas Turbines and Power,* **135**(091203), September, pp. 1 – 7.

[13] Henke, M., Klempp, N., Hohloch, M., Monz, T., and Aigner, M., 2015. "Validation of a T100 micro gas turbine steady-state simulation tool". In Proceedings of ASME Turbo Expo, no. GT2015-42090, Montreal, Canada, June 15 - 19, 2015.

[14] Krummrein, T., Henke, M., and Kutne, P., 2018. "A highly flexible approach on the steady-state analysis of innovative micro gas turbine cycles". In Proceedings of ASME Turbo Expo, no. GT2018-75664, Oslo, Norway, June 11-15, 2018. Manuscript submitted.

[15] Payri, F., Serrano, J., Fajardo, P., Reyes-Belmonte, M., and Gozalbo-Belles, R., 2012. "A physically based methodology to extrapolate performance maps of radial turbines". *Energy Conversion and Management,* **55**, mar, pp. 149–163.

[16] ICAO, 2011. Airport air quality manual - doc 9889. Tech. rep., International Civil Aviation Organization.

[17] Schürmann, G., Schäfer, K., Jahn, C., Hoffmann, H., Bauerfeind, M., Fleuti, E., and Rappenglück, B., 2007. "The impact of NOx, CO and VOC emissions on the air quality of zurich airport". *Atmospheric Environment,* **41**(1), pp. 103 – 118.

[18] Bundesministerium für Umwelt (BMU), 2002. TA-Luft: Erste Allgemeine Verwaltungsvorschrift zum Bundesimmissionsschutzgesetz.

[19] Joos, F., 2006. *Technische Verbrennung - Verbrennungstechnik, Verbrennungsmodellierung, Emissionen*. Springer-Verlag Berlin Heidelberg.

[20] Zanger, J., Monz, T., and Aigner, M., 2015. "Experimental investigation of the combustion characteristics of a double-staged FLOX-based combustor on an atmospheric and a micro gas turbine test rig". In Proceedings

of ASME Turbo Expo, no. GT2015-42313, Montreal, Canada, June 15 - 19, 2015.
[21] Chen, J., Mitchell, M. G., and Nourse, J. G., 2010. “Development of ultra-low emission diesel fuel-fired microturbine engines for vehicular heavy duty applications-combustion modifications”. In Proceedings of ASME Turbo Expo, no. GT2010-23181, Glasgow, UK, June 14 - 18, 2010.
[22] Gounder, J., Zizin, A., Lammel, O., and Aigner, M., 2016. “Spray characteristics measured in a new FLOX based low emission combustor for liquid fuels using laser and optical diagnostics”. In Proceedings of ASME Turbo Expo, no. GT2016-56629, Seoul, South Korea, June 13 - 17, 2016.

The original publication is available at http://dx.doi.org/10.1115/1.4041119